A&A 629, A33 (2019)
https://doi.org/10.1051/0004-6361/201935901

Astronomy & Astrophysics

Faint solar analogues at the limit of no reddening

Precise atmospheric parameters from moderate low-resolution spectra⋆

R. E. Giribaldi[1,2], G. F. Porto de Mello[2], D. Lorenzo-Oliveira[3], E. B. Amôres[4], and M. L. Ubaldo-Melo[2]

[1] ESO – European Southern Observatory, Karl-Schwarzchild-Strasse 2, 85748 Garching bei München, Germany
e-mail: rianoesc@gmail.com
[2] Observatório do Valongo, Universidade Federal do Rio de Janeiro, Ladeira do Pedro Antônio 43, 20080-090 Rio de Janeiro, RJ, Brazil
[3] Departamento de Astronomia do IAG/USP, Universidade de São Paulo, Rua do Matão 1226, Cidade Universitária, 05508-900 São Paulo, SP, Brazil
[4] UEFS, Departamento de Física, Av. Transnordestina, s/n, Novo Horizonte, Feira de Santana, CEP 44036-900, BA, Brazil

Received 16 May 2019 / Accepted 6 July 2019

ABSTRACT

Context. The flux distribution of solar analogues is required for calculating the spectral albedo of solar system bodies such as asteroids and trans-Neptunian objects. Ideally a solar analogue should be comparatively faint as the target of interest, but very few analogues fainter than $V = 9$ mag have been identified so far. Only atmospheric parameters equal to solar guarantee a flux distribution equal to solar as well, while only photometric colours equal to solar do not. Reddening is also a factor to consider when selecting faint analogue candidates.

Aims. Our aim is to implement the methodology for identifying faint analogues at the limit of precision allowed by the current spectroscopic surveys. We quantify the precision attainable for the atmospheric parameters of effective temperature ($T_{\rm eff}$), metallicity ([Fe/H]), and surface gravity (log g) when derived from moderately low-resolution ($R = 8000$) spectra with $S/N \sim 100$. We estimate the significance of reddening at 100–300 pc from the Sun.

Methods. We used the less precise photometry in the HIPPARCOS catalogue to select potential analogues with $V \sim 10.5$ mag (located at ∼135 pc). We calibrated $T_{\rm eff}$ and [Fe/H] as functions of equivalent widths of spectral indices by means of the principal component analysis regression. We derived log g, mass, radius, and age from the atmospheric parameters, *Gaia* parallaxes, and evolutionary tracks. We evaluated the presence of reddening for the candidates by underestimations of photometric $T_{\rm eff}$ with respect to those derived by spectral indices. These determinations were validated with extinction maps.

Results. We obtained the atmospheric parameters $T_{\rm eff}$, [Fe/H], and log g with precision of 97 K, 0.06 dex, 0.05 dex, respectively. From 21 candidates analysed, we identify five solar analogues: HIP 991, HIP 5811, and HIP 69477 have solar parameters within 1σ errors, and HIP 55619 and HIP 61835 within 2σ errors. Six other stars have $T_{\rm eff}$ close to solar, but slightly lower [Fe/H]. Our analogues show no evidence of reddening except for four stars, that present $E(B-V) \geq 0.06$ mag, translating to at least a 200 K decrease in photometric $T_{\rm eff}$.

Key words. techniques: spectroscopic – stars: solar-type – minor planets, asteroids: general – stars: fundamental parameters

1. Introduction

The Sun remains the primary and most fundamental reference object in stellar astrophysics. It is the golden standard for a variety of physical and chemical properties, and is still the sole star for which we access, both extensively and accurately, important fundamental parameters (Porto de Mello et al. 2014; Ramírez et al. 2009; Meléndez et al. 2006; Cayrel de Strobel 1996). On the one hand, the search for stars identical to the Sun in their physical properties, the so-called solar twins, has provided an interesting contextualization of the properties of the "Sun as a star": its age, chromospheric activity, and detailed chemical abundance (Meléndez et al. 2014; Li et al. 2012; Do Nascimento et al. 2009; Porto de Mello & da Silva 1997), among other quantities. On the other hand, a very relevant motivation to find and characterize stars that reproduce the solar spectrophotometric properties, something that solar twins are naturally expected to do, is the need to have reliable reference stars, observable at night under the same conditions as other targets of interest (Soubiran & Triaud 2004; Porto de Mello et al. 2014), hence the need to look for solar analogues, stars that closely reproduce the solar flux distribution, and may thus act as solar surrogates in the night sky.

According to the traditional definition of Cayrel de Strobel (1996), solar analogues are solar-type stars whose atmospheric parameters, namely effective temperature ($T_{\rm eff}$), metallicity ([Fe/H][1]), and surface gravity (log g), are similar to those of the Sun within specified uncertainty criteria, and therefore they present a solar flux distribution. Stars with photometric colours equal to solar are sometimes called solar analogues in the literature, but we note that the use of this working definition should be used with care because solar photometric colours alone do not necessarily imply a solar flux distribution. This is the reason why

⋆ Based on observations collected at Observatório do Pico dos Dias (OPD), operated by the Laboratório Nacional de Astrofísica, CNPq, Brazil and on data from the ESO Science Archive Facility.

[1] $[A/B] = \log\left(\frac{N(A)}{N(B)}\right)_{\rm Star} - \log\left(\frac{N(A)}{N(B)}\right)_{\rm Sun}$, where N denotes the number abundance of a given element.

the atmospheric parameters must be proven to be solar by spectroscopic techniques. Solar analogues may serve as calibrating objects when the solar flux distribution needs to be observed at night, that is, they may serve as solar proxies or solar surrogates. Ideally they should be known to magnitudes comparatively faint to the targets of interest in order to record the instrumental signature in the spectra of both the target and the proxy. Furthermore, the availability of a list of solar analogues well spread in the sky allows the users to choose a solar proxy close to the target, that can be observed with a similar airmass to record the same telluric features as in the target's spectrum. A proper solar proxy then guarantees the complete removal of the solar signature, of the instrumental signature, and of the telluric features, which is essential for recovering accurately the body's albedo, whose shape and inclination are used for taxonomy (e.g., Chapman et al. 1975; Tholen & Barucci 1989). Since solar system bodies such as trans-Neptunian objects with $V \sim 15$ mag or fainter are routinely observed nowadays, it is reasonable to require solar proxies with $V =$ 13–14 mag for example. Such proxies are at least ten times brighter than common targets, but should still allow convenient corrections.

Porto de Mello et al. (2014) has recently provided a sizable list of solar analogues, characterized both photometrically and spectroscopically, and well distributed in the night sky, widely extending both in quality and quantity the initial work of Hardorp (1982), who provided the first impetus on the search for solar analogues. Surprisingly, Hardorp's lists are still referred to nowadays. However, the lists of Porto de Mello et al. (2014) reach no fainter than $V = 9$ mag, not much better than Hardorp's, only sampling stars within 50 pc of the Sun. This magnitude range is too bright for telescopes of the 8–10 m class. An example that illustrates the need for fainter solar analogues is the use of the stars BD+00 3383 ($V = 10.50$ mag) and HD 11532 ($V = 9.71$ mag). They both showed acceptable performances as solar proxies although no detailed spectroscopy was applied to them to determine their atmospheric parameters. They were used to recover albedos from the infrared to the visible (e.g. Merlin et al. 2017; Dumas et al. 2011; Alvarez-Candal et al. 2008), and the UV (e.g., Snodgrass et al. 2017). For a solar-type star, the flux variation as a function of the atmospheric parameters from the infrared to the visible keeps a nearly constant shape, but this no longer applies from λ5000 Å downwards to the UV, a region much more sensitive to $T_{\rm eff}$, [Fe/H], and log g shifts, in this order. For example, Fig. 1 in Fernley et al. (1996) shows that a variation of −200 K from the solar $T_{\rm eff}$ increases the flux by ∼15% at 4000 Å with respect to that at 5000 Å. In cases like this, solar analogues with atmospheric parameters very close to solar are advisable in order to assert the minimum influence on the intrinsic shape of the target's albedo.

In the present work we implement methods to identify faint solar analogues. The definition of "faint" is subjective because it has to conform to the requirements of the users or to the faintest analogues identified so far. For example, stars that were considered faint in the HIPPARCOS catalogue are definitely not so for present *Gaia* standards; 20 yr of technological advances allow much deeper sky prospecting. Since we are hunting for solar analogues, the definition of faint we adopt conforms to the apparent magnitude of the stars whose photometric, astrometric, and spectroscopic available data have the minimum quality to determine their atmospheric parameters with reasonable precision: 100 K, 0.05 dex, and 0.05 dex respectively in $T_{\rm eff}$, [Fe/H], and log g. We employed data from HIPPARCOS as our initial screening; these data are not now current, though they were so at the time our survey started. Much more precise photometric and astrometric data were made available by *Gaia* (Gaia Collaboration 2016a). However, the stars with the less precise photometry in HIPPARCOS, close to this catalogue's completeness limit, those with $V \sim 10.5$ mag, are still competitive as reasonably faint solar analogues. The methods implemented here can be readily applied to spectra with similar characteristics acquired by telescopes of 8–10 m, corresponding to stars of $V = 16$–18 mag.

Interstellar extinction arises as an additional problem for the selection of candidates as they become increasingly fainter and farther away. Solar analogues are most probably located in the Galactic thin disk because the metallicity distribution of this population is essentially solar (e.g., Adibekyan et al. 2013). The scale height of the thin disk is estimated at ∼300 pc (Jurić et al. 2008, and references therein), thus at longer distances a more productive search could be performed by pointing to the Galactic plane than to the poles. At the same time, pointing to the plane implies candidates with more attenuated magnitudes and more reddened colours, thus precise corrections for Galactic layers must be applied. These solar analogues will probably not satisfy the need for solar surrogates, either photometrically or spectroscopically, from the blue limit of the H band to shorter wavelengths because extinction increases quickly from there (e.g., Gordon et al. 2003, Fig. 10).

Some faint solar analogues and twins have already been identified, for example Inti 1 with $V = 12.86$ mag (Galarza et al. 2016), KIC 10971974 with $V = 11.05$ mag (Beck et al. 2017), and those in the M67 cluster with $V \sim 14.60$ mag (Pasquini et al. 2008; Önehag et al. 2011). Here we provide a short list of solar analogues found when testing our methods. They should subsequently undergo more precise spectroscopic analyses to better determine their fundamental parameters and to derive other quantities such as rotation, detailed chemical composition, magnetic activity, and asteroseismological properties.

This paper is organized as follows. In Sect. 2 we describe the selection criterion of the candidates. In Sect. 3 we describe the data reduction. In Sect. 4 we describe the principal component analisis (PCA) regression applied to spectral indices. In Sect. 5 we present the fundamental parameters derived for the candidates. In Sect. 6 we determine the influence of reddening on photometric colours. In Sect. 7 we summarize the information obtained for the best solar analogues identified, and finally in Sect. 8, we present our conclusions.

2. Selecting the sample of faint analog candidates

This survey was launched at the time the HIPPARCOS catalogue (Perryman et al. 1997) was the reference for the most precise parallaxes, colours, and magnitudes for solar-type stars, and the procedure we employed takes this into consideration.

We started our search by selecting candidates according to colour (proxies of $T_{\rm eff}$ and [Fe/H]) and absolute magnitude (proxy of log g), the observable quantities that allow a broad selection. The colours in widespread use and with several available $T_{\rm eff}$ calibrations are $B-V$ and $(B-V)^{\rm Ty}$ from the Johnson and *Tycho* (Hoeg et al. 1997) systems. The initial procedure follows closely that used in Porto de Mello et al. (2014): "boxes" were prospected around the solar colours and absolute magnitudes $(B-V)_\odot = 0.654$ mag, $(B-V)^{\rm Ty}_\odot = 0.733$ mag, $M_{V_\odot} = 4.82$ mag, $M^{\rm Ty}_{V_\odot} = 4.88$ mag. HIPPARCOS is complete up to $V \sim 9$ mag, but still lists fainter stars in decreasing degrees of completeness down to $V \sim 11$ mag. We chose HIPPARCOS for the sample

selection because it has more precise parallaxes than *Tycho*, which permits a more reliable selection based on magnitudes, although *Tycho* goes deeper, being complete down to $V^{\rm Ty} = 10$ mag and still 90% complete down to $V^{\rm Ty} \sim 10.5$ mag.

The final list of candidates to be analysed spectroscopically should have a size compatible with the accomplishment of this project in the Observatório Pico dos Dias (OPD) operated by the Laboratório Nacional de Astrofisica (LNA) and the Brazilian National Council for Scientific and Technologial Development (CNPq) within a period of a few years. These practical order considerations constrain the candidate list to some tens of objects at most. We note, however, that while we used HIPPARCOS for the sample selection, the determination of log g, mass, radius, age, and reddening were updated with the parallaxes of *Gaia* DR2 (Gaia Collaboration 2016a, 2018).

We started with some rough tests to gauge the size of the sample. Solar-type stars were considered with V between 10.5 and 11.2 mag, the faint limit of HIPPARCOS. The dimensions of the boxes around the solar colours and absolute magnitudes were set by the mean of the 1σ errors of all stars contained within the box, self-consistently. We worked simultaneously with boxes around the Johnson and *Tycho* solar colours and absolute magnitudes, and we kept stars within 2σ of the box centres. The average uncertainties of colour and absolute magnitude for the stars contained in the box are very similar to the uncertainty values used to define the boxes in the first place, the representative uncertainties are as follows:

$\langle\sigma(B-V)\rangle = 0.07$ mag,
$\langle\sigma(B-V)^{\rm Ty}\rangle = 0.12$ mag,
$\langle\sigma(M_V)\rangle = 0.80$ mag,
$\langle\sigma(M_V)^{\rm Ty}\rangle = 0.80$ mag.

These tests constrained samples of around 300 stars, which we decreased by considering only those objects, within these initial 2σ boxes defined by average errors, for which the individual uncertainty implied a 2σ agreement with the solar values defining the centres of the boxes. This second sample totalled 203 stars, with the following average errors:

$\langle\sigma(B-V)\rangle = 0.067$ mag,
$\langle\sigma(B-V)^{\rm Ty}\rangle = 0.112$ mag,
$\langle\sigma(M_V)\rangle = 0.609$ mag,
$\langle\sigma(M_V)^{\rm Ty}\rangle = 0.682$ mag.

Finally, we fine tuned this subsample by retaining only those objects for which the individual errors were no larger than the average errors defined for each box, thus a 1σ criterion, applying the cuts stepwise in the $M_{V_\odot}$, $M^{\rm Ty}_{V_\odot}$, $(B-V)^{\rm Ty}_\odot$, and $(B-V)_\odot$ dimensions, in this order. We have purposefully disregarded reddening in the selection process in order to gauge its influence on the method of selection.

The selected candidate sample contains 41 stars, which are listed in Table 1. The table gives the stellar photometric and astrometric measurements as shown in the HIPPARCOS, Two Micron All Sky Survey (Cutri et al. 2003), and *Gaia* DR2 catalogues. The table is divided in two parts; the first lists the observed stars (hereafter "candidates") for which the S/N is noted. We also show in Fig. 1 the spatial distribution of the candidates in Galactic coordinates. No candidates are located towards the Galactic plane, thus their reddening is expected to be low, although some exceptions as found (see Sect. 6).

3. Observations and data reduction

Spectroscopic observations were performed with the long-slit coudé spectrograph, coupled to the 1.60 m OPD telescope in six missions from 1998–2013. The spectra cover a range of 500 Å centred in λ6563 Å (Hα), and have a nominal resolution of $R = \lambda/\Delta\lambda \sim 8000$. The signal-to-noise ratio (S/N) of the spectra ranges between 70 and 220 for the candidates, and between 70 and 810 for the calibration stars (see Tables 1 and A.1, respectively).

The data reduction was carried out by the standard procedure using IRAF[2], i.e. for one-dimensional spectra extraction, bias and flat-field corrections were performed prior to background and scattered light subtraction. The pixel-to-wavelength calibration was obtained by comparing the spectra of stars with a thorium-argon lamp spectra acquired on the same night of the observations. Doppler corrections were applied for all spectra and continuum normalizations were performed by fitting low-order polynomials to the highest flux regions following a systematic procedure.

4. Calibration of spectral indices

In order to determine the atmospheric parameters of the candidates, we built a calibration by means of the principal component analysis (PCA) applied to the equivalent width (EW) of the spectral indices. At $R = 8000$, individual metallic lines are not resolved, thus, the determination of atmospheric parameters using spectroscopic techniques such as the excitation and ionization equilibrium of Fe lines, and Balmer-line fitting is not possible. Alternatively, spectral indices have been validated as competitive in this task using intermediate quality spectra (e.g. Ghezzi et al. 2014).

4.1. Calibration stars

We observed a sample of 69 solar-type stars in order to calibrate the spectral indices (hereafter calibration stars), and are listed in Table A.1. Their atmospheric parameters were extracted from the literature, and the sources are provided in the table. Most of the sample (39 stars) is found in Ghezzi et al. (2010a,b), where $T_{\rm eff}$ determinations are based on excitation and the ionization equilibrium of Fe lines. The rest of the stars belong to catalogues where $T_{\rm eff}$ was derived by the same technique, except for 16 stars whose parameters were extracted from Porto de Mello et al. (2014) where $T_{\rm eff}$ is the average of photometric calibrations and Hα line-profile fitting. The mean quoted precision of this sample is ~40 K, 0.02 dex, and 0.10 dex respectively in $T_{\rm eff}$, [Fe/H], and log g. Ten stars were observed twice with the purpose of estimating uncertainties of the index measurements: HD 146233, HD 150248, HD 112164, HD 131117, HD 34721, HD 20029, HD 206395, HD 212330, HD205420, and HD 215648.

The distribution of the calibration stars in the parameter space is shown in Fig. 2. They are more densely packed around the solar parameters $T_{\rm eff} = 5772$ K (Prša et al. 2016; Heiter et al. 2015), [Fe/H] = 0 dex, and $\log g = 4.44$ dex to calibrate as precisely as possible the area of solar analogues. We note that the area for $T_{\rm eff} < 5600$ K is practically empty. This highlights

[2] Image Reduction and Analysis Facility (IRAF) is distributed by the National Optical Astronomical Observatories (NOAO), which is operated by the Association of Universities for Research in Astronomy (AURA), Inc., under contract to the National Science Foundation (NSF).

Table 1. Photometric and astrometric data of the candidates.

HIP	RA	Dec	$(B-V)$	$(B-V)^{Ty}$	V	J	H	K_s	Parallax (mas)	S/N
991	00 : 12 : 18	−40 : 38 : 44	0.600 ± 0.061	0.647 ± 0.070	10.58 ± 0.047	9.476 ± 0.026	9.136 ± 0.026	9.067 ± 0.024	7.0441 ± 0.0326	108
5811	01 : 14 : 33	−49 : 54 : 12	0.700 ± 0.004	0.767 ± 0.090	10.62 ± 0.055	9.458 ± 0.032	9.106 ± 0.033	9.077 ± 0.033	7.5506 ± 0.0271	112
6089	01 : 18 : 11	−27 : 36 : 17	0.661 ± 0.015	0.647 ± 0.094	10.55 ± 0.061	9.353 ± 0.030	8.990 ± 0.076	8.912 ± 0.019	8.7481 ± 0.0412	126
8853	01 : 53 : 51	−23 : 29 : 52	0.530 ± 0.020	0.563 ± 0.083	10.63 ± 0.058	9.672 ± 0.024	9.408 ± 0.022	9.404 ± 0.023	5.2837 ± 0.0386	90
10663	02 : 17 : 13	−24 : 23 : 56	0.570 ± 0.020	0.522 ± 0.100	10.62 ± 0.072	9.615 ± 0.023	9.379 ± 0.022	9.289 ± 0.021	3.6740 ± 0.0386	121
13964	02 : 59 : 49	−11 : 20 : 42	0.556 ± 0.015	0.548 ± 0.093	10.53 ± 0.065	9.457 ± 0.023	9.058 ± 0.022	8.967 ± 0.020	9.0105 ± 0.0560	210
18941	04 : 03 : 36	−36 : 10 : 40	0.590 ± 0.020	0.564 ± 0.078	10.52 ± 0.055	9.376 ± 0.027	9.093 ± 0.024	9.005 ± 0.021	7.0380 ± 0.0221	114
24742	05 : 18 : 19	−48 : 52 : 12	0.529 ± 0.032	0.518 ± 0.091	10.67 ± 0.063	9.514 ± 0.029	9.167 ± 0.022	9.095 ± 0.021	7.1532 ± 0.0184	103
29100 (*)	06 : 08 : 17	−30 : 40 : 05	0.611 ± 0.003	0.657 ± 0.081	10.56 ± 0.053	9.429 ± 0.022	9.092 ± 0.022	9.054 ± 0.019	7.8400 ± 0.2100	134
31845	06 : 39 : 30	−31 : 25 : 50	0.626 ± 0.015	0.777 ± 0.086	10.51 ± 0.052	9.191 ± 0.023	8.832 ± 0.044	8.789 ± 0.024	9.0866 ± 0.0241	112
48272	09 : 50 : 29	−04 : 57 : 37	0.536 ± 0.003	0.595 ± 0.107	10.51 ± 0.072	9.387 ± 0.023	9.096 ± 0.023	8.997 ± 0.020	7.3291 ± 0.0359	92
55619	11 : 23 : 43	−25 : 06 : 30	0.667 ± 0.004	0.762 ± 0.092	10.55 ± 0.058	9.344 ± 0.027	8.937 ± 0.026	8.884 ± 0.021	7.6182 ± 0.0409	121
56870	11 : 39 : 34	−14 : 04 : 34	0.645 ± 0.003	0.872 ± 0.095	10.53 ± 0.055	9.260 ± 0.024	8.931 ± 0.023	8.839 ± 0.024	9.2905 ± 0.0356	122
61835	12 : 40 : 17	+27 : 46 : 34	0.588 ± 0.015	0.527 ± 0.103	10.80 ± 0.073	9.719 ± 0.023	9.427 ± 0.027	9.373 ± 0.022	5.5279 ± 0.0527	143
67692	13 : 51 : 59	+26 : 38 : 11	0.750 ± 0.015	0.906 ± 0.102	10.94 ± 0.060	9.587 ± 0.022	9.204 ± 0.019	9.139 ± 0.022	3.4312 ± 0.0612	92
69232	14 : 10 : 27	−13 : 56 : 04	0.605 ± 0.025	0.647 ± 0.107	10.67 ± 0.071	9.404 ± 0.023	9.055 ± 0.022	8.961 ± 0.024	7.1930 ± 0.0500	81
69477	14 : 13 : 25	+23 : 54 : 03	0.562 ± 0.066	0.603 ± 0.075	10.53 ± 0.052	9.307 ± 0.019	9.010 ± 0.021	8.960 ± 0.024	8.2887 ± 0.0321	114
73234	14 : 58 : 03	+09 : 24 : 03	0.680 ± 0.061	0.743 ± 0.077	10.59 ± 0.050	9.448 ± 0.023	9.143 ± 0.023	9.078 ± 0.023	5.3550 ± 0.0761	87
75685	15 : 27 : 42	−02 : 45 : 18	0.730 ± 0.015	0.872 ± 0.099	10.51 ± 0.060	9.186 ± 0.024	8.870 ± 0.042	8.810 ± 0.024	6.3801 ± 0.0337	72
107605	21 : 47 : 41	−41 : 51 : 17	0.640 ± 0.020	0.664 ± 0.090	10.60 ± 0.060	9.498 ± 0.022	9.243 ± 0.027	9.180 ± 0.021	6.4888 ± 0.0456	170
111826	22 : 39 : 01	+32 : 18 : 03	0.762 ± 0.065	0.850 ± 0.086	10.53 ± 0.053	9.216 ± 0.027	8.817 ± 0.026	8.796 ± 8.786	8.4807 ± 0.0326	125
13 052	02 : 47 : 45	+80 : 15 : 54	0.784 ± 0.062	0.899 ± 0.080	10.53 ± 0.047	9.155 ± 0.022	8.811 ± 0.029	8.711 ± 0.025	11.1187 ± 0.0436	–
16 294	03 : 30 : 03	+51 : 30 : 43	0.520 ± 0.020	0.729 ± 0.086	10.56 ± 0.054	9.337 ± 0.020	9.119 ± 0.026	9.053 ± 0.020	5.4415 ± 0.0526	–
17 514	03 : 45 : 00	−38 : 51 : 33	0.598 ± 0.015	0.782 ± 0.010	10.64 ± 0.063	9.447 ± 0.021	9.111 ± 0.024	9.017 ± 0.023	7.6114 ± 0.0324	–
46 072	09 : 23 : 41	+65 : 48 : 31	0.675 ± 0.044	0.737 ± 0.055	10.53 ± 0.035	9.329 ± 0.020	9.062 ± 0.017	8.979 ± 0.016	7.0718 ± 0.0272	–
53 442	10 : 55 : 58	+29 : 19 : 13	0.552 ± 0.067	0.592 ± 0.076	10.51 ± 0.051	9.362 ± 0.021	9.041 ± 0.016	8.955 ± 0.018	7.5127 ± 0.0845	–
53 990	11 : 02 : 39	−32 : 44 : 17	0.550 ± 0.020	0.732 ± 0.090	10.67 ± 0.057	9.553 ± 0.024	9.336 ± 0.024	9.229 ± 0.021	5.3337 ± 0.0431	–
55 229	11 : 18 : 36	+50 : 44 : 55	0.688 ± 0.062	0.753 ± 0.078	10.76 ± 0.048	9.580 ± 0.022	9.269 ± 0.028	9.235 ± 0.023	4.4272 ± 0.0394	–
55 809	11 : 26 : 11	+53 : 32 : 39	0.654 ± 0.049	0.729 ± 0.065	10.50 ± 0.042	9.257 ± 0.019	9.001 ± 0.031	8.852 ± 0.022	5.3923 ± 0.0330	–
59 223	12 : 08 : 47	+30 : 56 : 33	0.542 ± 0.065	0.580 ± 0.074	10.51 ± 0.051	9.464 ± 0.022	9.220 ± 0.021	9.162 ± 0.017	6.2389 ± 0.0398	–
59 369	12 : 10 : 49	+32 : 44 : 54	0.573 ± 0.067	0.615 ± 0.076	10.58 ± 0.051	9.523 ± 0.027	9.174 ± 0.028	9.191 ± 0.019	5.5150 ± 0.0364	–
60 523	12 : 24 : 25	+53 : 26 : 54	0.680 ± 0.055	0.743 ± 0.069	10.77 ± 0.043	9.650 ± 0.027	9.356 ± 0.026	9.261 ± 0.018	6.3396 ± 0.0294	–
61 957	12 : 41 : 51	+26 : 49 : 47	0.585 ± 0.015	0.511 ± 0.075	10.54 ± 0.052	9.540 ± 0.023	9.264 ± 0.021	9.220 ± 0.020	4.4171 ± 0.1482	–
63 588	13 : 01 : 51	+27 : 20 : 15	0.594 ± 0.015	0.802 ± 0.112	10.70 ± 0.069	9.525 ± 0.026	9.271 ± 0.034	9.131 ± 0.020	6.0707 ± 0.0460	–
67 215	13 : 46 : 26	+82 : 31 : 46	0.695 ± 0.065	0.783 ± 0.086	10.52 ± 0.054	9.474 ± 0.020	9.222 ± 0.017	9.157 ± 0.017	6.2334 ± 0.0259	–
69 554	14 : 14 : 14	+38 : 19 : 58	0.723 ± 0.066	0.819 ± 0.087	10.79 ± 0.053	9.568 ± 0.020	9.256 ± 0.016	9.209 ± 0.016	7.2600 ± 0.0256	–
73 854	15 : 05 : 37	+45 : 23 : 49	0.724 ± 0.064	0.800 ± 0.083	10.53 ± 0.052	9.435 ± 0.021	9.164 ± 0.019	9.098 ± 0.020	7.3037 ± 0.0241	–
74 061	15 : 08 : 09	+39 : 58 : 12	0.633 ± 0.064	0.700 ± 0.085	10.58 ± 0.055	9.462 ± 0.021	9.098 ± 0.021	9.008 ± 0.014	5.3679 ± 0.0723	–
76 272	15 : 34 : 45	+62 : 16 : 44	0.592 ± 0.065	0.637 ± 0.075	10.52 ± 0.051	9.684 ± 0.021	9.315 ± 0.017	9.216 ± 0.020	6.2103 ± 0.0269	–
102 416	20 : 45 : 13	+60 : 19 : 35	0.642 ± 0.064	0.712 ± 0.085	10.52 ± 0.055	9.341 ± 0.023	9.027 ± 0.031	8.970 ± 0.019	7.8116 ± 0.0293	–
110 560	22 : 23 : 49	+24 : 23 : 34	0.573 ± 0.016	0.773 ± 0.097	10.64 ± 0.059	9.440± 0.022	9.172 ± 0.021	9.106 ± 0.018	5.0932 ± 0.0383	–

Notes. Stars for which no S/N is given in Col. 11 were photometrically selected, but not spectroscopically observed. The first column lists the HIPPARCOS number. Columns 2 and 3 display the coordinates, right ascension and declination. Columns 4 and 5 list $B-V$ in Johnson and *Tycho* systems. Columns 6–9 list the magnitudes in the indicated photometric bands. V was extracted from the HIPPARCOS catalogue to which we associated with the error of the same band in the *Tycho* system. Column 10 lists parallaxes from *Gaia* DR2 (Gaia Collaboration 2018). Column 11 lists the S/N of the acquired spectra. (*)The parallax of this candidate was extracted from the *Gaia* DR1 catalog (Gaia Collaboration 2016a,b).

the applicability limitation of our method, especially towards cooler and metal-poor stars. Therefore, we adopt the applicability range of our calibrations as follows: $5600 \leq T_{\rm eff} \leq 6300$ K, $-0.3 \leq$ [Fe/H] ≤ 0.4 dex, $\log g \geq 4.1$ dex.

4.2. Identification of indices

Following Ghezzi et al. (2014) we only selected indices dominated by iron peak elements, from both neutral and ionized species, with a contribution of more than 90% – (Fe I, Fe II, Ti II, V I, Cr I, Cr II, Mn I, Co I, Ni I). These indices are shown to best correlate with atmospheric parameters. The inspection was carried out along the available spectral range avoiding the Hα profile.

Line identification was performed by comparing simultaneously the Kitt Peak National Observatory solar atlas (KPNO; Kurucz 2005)[3] with spectra of the Sun (reflected off Ganymede), HD 19637, and HD 182572 (see Fig. 3). The comparison between KPNO and Ganymede helps to visually identify metallic lines in the indices; their contributions were estimated by their EWs,

[3] http://kurucz.harvard.edu/sun/fluxatlas2005/

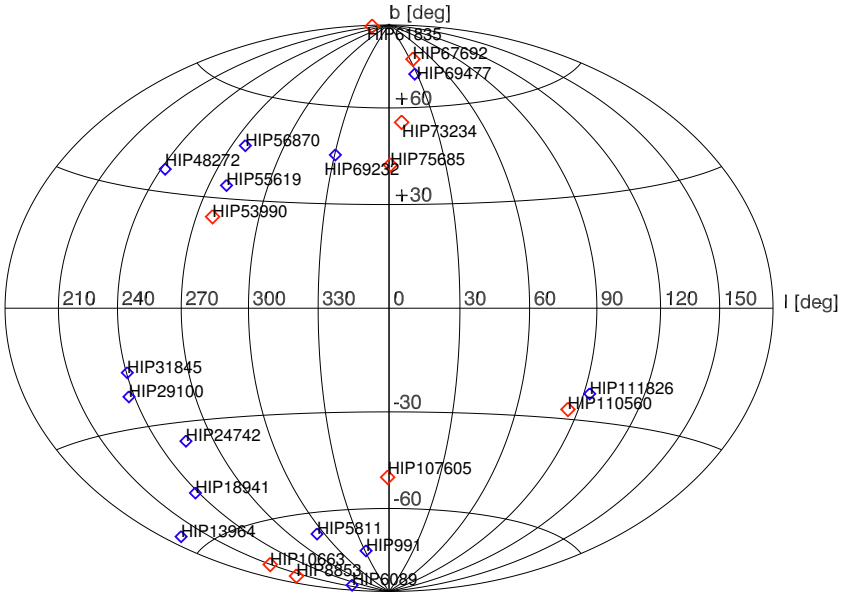

Fig. 1. Distribution of candidates in Galactic coordinates. Stars with distances <150 pc are the blue diamonds, and those with distances >150 pc are the red diamonds.

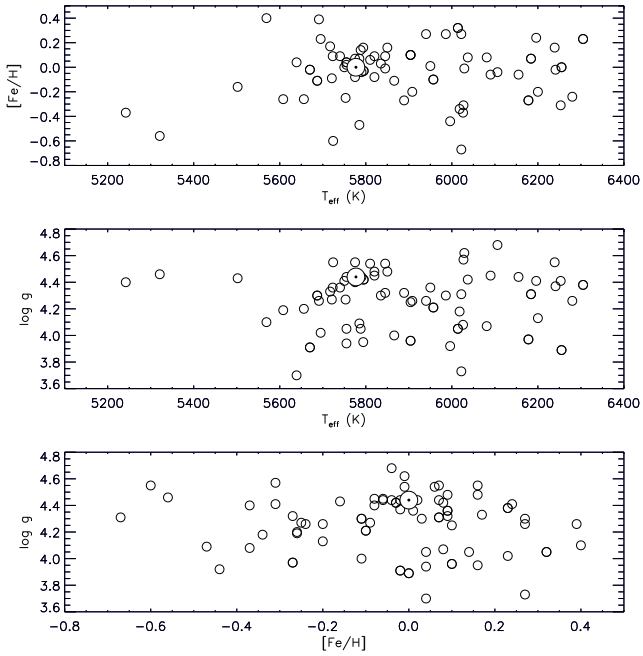

Fig. 2. Distribution of the atmospheric parameters of the calibration stars around the solar values. The solar parameters are represented by the circled dot symbol ⊙.

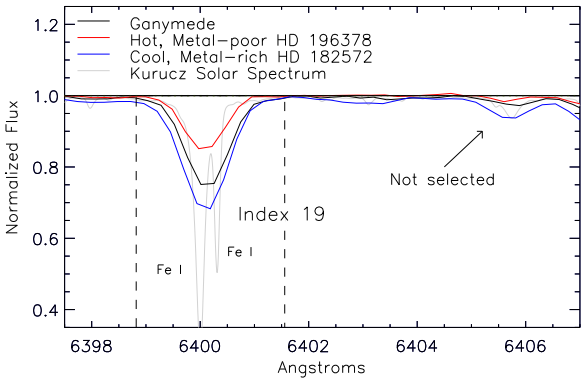

Fig. 3. Definition of one spectral index. The KPNO atlas with resolution $R = 500\,000$ is shown in grey. The other spectra with resolution $R = 8000$ are from the Sun (black), HD 196378 (red), and HD 182572 (blue). The dashed lines indicate the boundaries of index 19, formed by two Fe I lines.

as listed in the catalogue of Moore et al. (1966). The element species were also checked using the VALD3 database (Ryabchikova et al. 2015). The spectrum of HD 19637 (a hot, metal-poor star) was used to dismiss the weakest indices, while the spectrum of HD 182572 (a cool, metal-rich star) was used to better define the wavelength limits of the indices. We selected 42 well-defined indices that were submitted to the sensitivity test described below.

4.3. Calibration by PCA

Correlations of the EWs of the indices with the atmospheric parameters $T_{\rm eff}$, [Fe/H], and log g are approximated by a Taylor polynomial expansion of second order, as follows:

$$\begin{aligned}\mathrm{EW\ (mÅ)} = {} & c_0 + c_1[\mathrm{Fe/H}] + c_2 T_{\rm eff} + c_3 \log g \\ & + c_4[\mathrm{Fe/H}]T_{\rm eff} + c_5[\mathrm{Fe/H}]\log g + c_6 T_{\rm eff}\log g \\ & + c_7([\mathrm{Fe/H}])^2 + c_8(T_{\rm eff})^2 + c_9(\log g)^2. \end{aligned} \quad (1)$$

Following the same procedures of Ghezzi et al. (2014), we select 24 indices with the best sensitivity to $T_{\rm eff}$ and [Fe/H] (class 1 and 2, according to their definition), to which we then applied the PCA regression.

The PCA extracts important information from the correlated data sets, in which the direction of the greater variability of the correlations is searched. It finds a new basis in which the data sets exhibit their greatest variance, providing groups of non-correlated orthogonal components (principal components, PCs) based on linear combinations of the original input variables (the spectral index EWs in our case). This approach enables the extraction of the most relevant combinations of the original input variables, and thus they can be used for the efficient discrimination of objects of different natures that present similar observables (e.g. Blanco-Cuaresma et al. 2015; Hunt et al. 2012),

and can be also calibrated against physically motivated variables, such as $T_{\rm eff}$, [Fe/H], and log g, as done in Muñoz Bermejo et al. (2013), and as we do in the present work.

The variables were standardized to take into account their different scales as

$$\text{Variable} = \frac{\text{Variable} - \langle\text{Variable}\rangle}{\sigma(\text{Variable})}, \quad (2)$$

where $\langle$Variable$\rangle$ and σ(Variable) are, respectively, its average and standard deviation. We explored the correlations between the PCs and the atmospheric parameters of our calibration sample finding that the first and second principal components (PC1 and PC2) are better related to all three parameters, i.e. they correspond to 90% of the total cumulative variance of the data. The other higher order principal components do not show significant correlation with the atmospheric parameters and thus were discarded. We used the best regressive model to build a calibration for each one of the atmospheric parameters. Equations (3)–(5), show the atmospheric parameters as functions of PC1 and PC2:

$$T_{\rm eff} = 5913(\pm12) + 18(\pm3)\text{PC1} - 124(\pm9)\text{PC2} - 7(\pm3)(\text{PC1}\times\text{PC2}), \quad (3)$$

$$[\text{Fe/H}] = -0.01(\pm0.01) - 0.039(\pm0.0)\text{PC1} - 0.042(\pm0.0)\text{PC2}, \quad (4)$$

$$\log g = 4.30(\pm0.03) - 0.0(\pm0.01)\text{PC1} + 0.06(\pm0.02)\text{PC2} - 0.01(\pm0.01)(\text{PC1}\times\text{PC2}). \quad (5)$$

The internal uncertainties of these analyses are 93 K, 0.06 dex, and 0.16 dex, for each atmospheric parameter, $T_{\rm eff}$, [Fe/H], and log g, respectively.

5. Fundamental parameters of the candidates

5.1. Spectroscopic effective temperature and metallicity

We call "spectroscopic parameters" those derived from the PCA calibration of spectral indices, and we denote them hereafter as $T_{\rm eff}^{\rm PCA}$, [Fe/H]$^{\rm PCA}$, and log $g^{\rm PCA}$. The adopted values and uncertainties of stellar atmospheric parameters were estimated from 10^5 Monte Carlo (MC) simulations, assuming that the EWs errors follow Gaussian distributions. The fractional EW errors estimated from the subsample of stars with two observations are found to be ~4% (see Table A.1). The outcome of MC simulations are EW distributions that were propagated by Eqs. (3)–(5) to finally obtain a distribution of atmospheric parameters from which the most probable values and their errors were associated with the medians and standard deviations.

We applied this procedure to the calibration sample in order to check the consistency between the PCA-based parameters and those in the literature; the results are shown in Fig. 4. The agreement is satisfactory only for $T_{\rm eff}$ and [Fe/H]. Accordingly, log g values derived by spectral indices are dismissed, and we determine them by evolutionary tracks in Sect. 5.5. The plots confirm that the stars with parameters outside of the applicability range are biased (red squares) to hotter and more metal-rich diagnostics, in general. The plots also show that the spectroscopic PCA parameters of the only calibration star with a spectrum of $S/N < 100$ (a value representative of the candidate star sample) agree with the literature values. Literature $T_{\rm eff}$ values of the outlier HD 206860 (red triangle) were reviewed; the initially adopted $T_{\rm eff}$ was found to be too hot, being actually the hottest one in the published range.

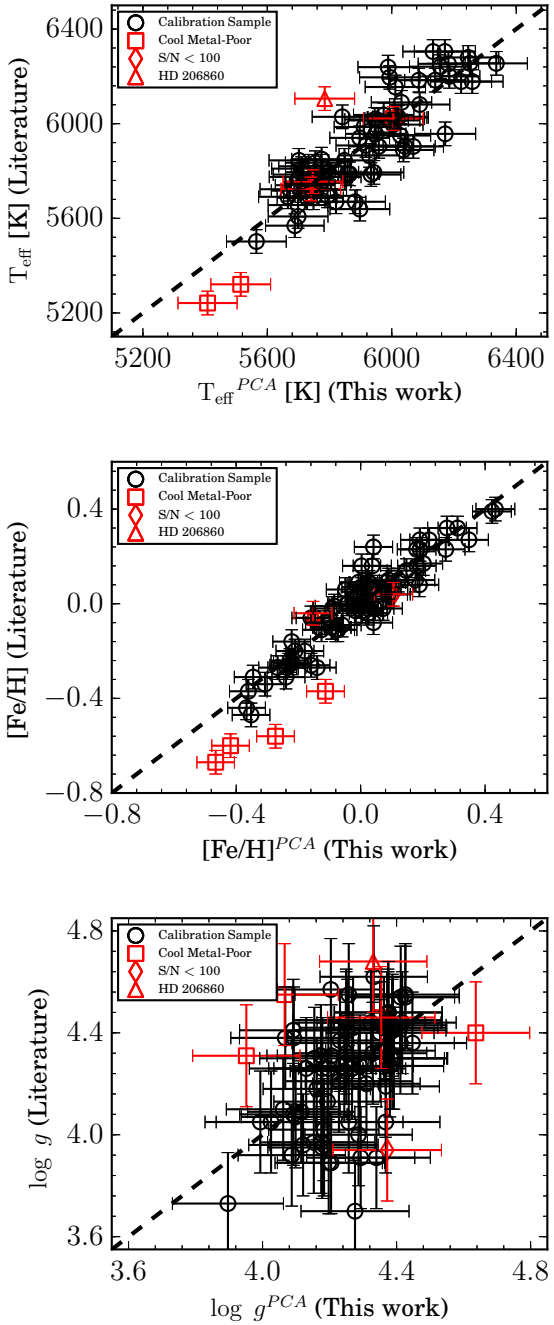

Fig. 4. Comparison between the atmospheric parameters from the literature and those from our PCA calibration.

The atmospheric parameters of the candidates derived by the procedures described above are presented in Table 1. We keep the notation $T_{\rm eff}^{\rm PCA}$ for temperatures derived by spectral indices, and the values presented in the table were corrected by the equation given in Sect. 5.3. Only parameters within the range of applicability pointed out in Sect. 4.1 are provided.

5.2. IRFM-photometric effective temperature

We derived another set of temperatures using the metallicity-dependent colour calibrations of Casagrande et al. (2010) based on the InfraRed Flux Method (IRFM; Blackwell & Shallis 1977; Blackwell et al. 1979, 1980) (hereafter $T_{\rm eff}^{\rm phot}$). Casagrande et al. (2010) corrected the systematics of previous

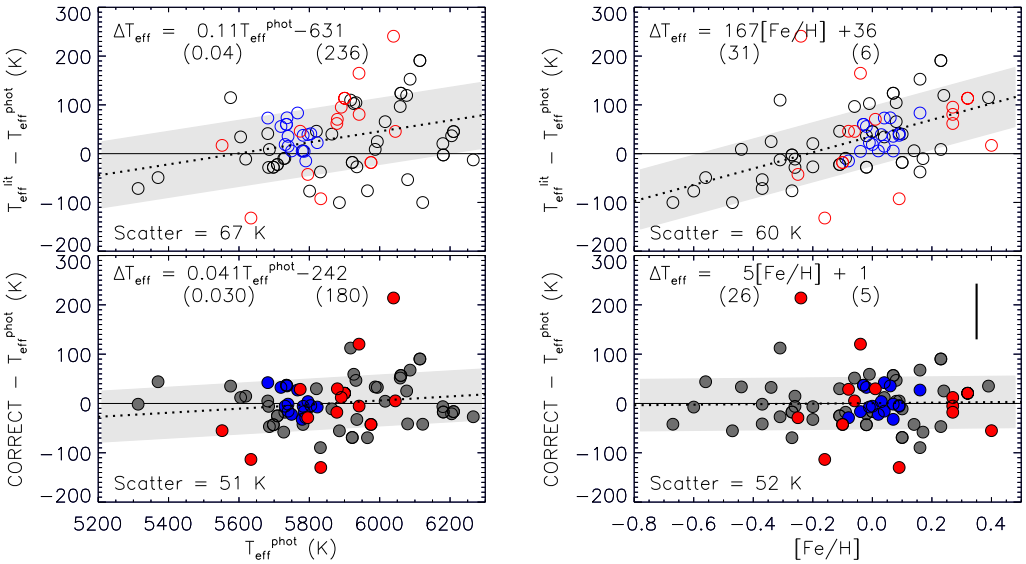

Fig. 5. *Top panels*: comparison between effective temperatures of the literature $T_{\rm eff}^{\rm lit}$ and $T_{\rm eff}^{\rm phot}$ of the calibration stars. Dark circles are the stars from Ghezzi et al. (2010a,b), blue circles are the stars from Porto de Mello et al. (2014), and red circles are the stars from all other sources listed in Table A.1. The dotted lines and the shaded areas are the trends and the 1σ dispersion around them, respectively; the equations are shown along with the errors of their coefficients in brackets. *Bottom panels*: same as in the top panels, but for $T_{\rm eff}^{\rm lit}$ corrected by $T_{\rm eff}^{\rm phot} = (T_{\rm eff}^{\rm lit} + 410)/1.08 - 153$[Fe/H] + 22. The vertical bar represents the mean uncertainties of the spectroscopic and photometric temperatures added: 40 + 73 K.

IRFM implementations; their temperature scale was found to be in precise agreement with $T_{\rm eff}$ derived from interferometric measurements for the metallicity range in this work (Casagrande et al. 2014; Giribaldi et al. 2019). Thus, we consider the $T_{\rm eff}^{\rm phot}$ as the standard scale.

We derived $T_{\rm eff}^{\rm phot}$ by computing the weighted mean of the temperatures obtained with the $(B-V)$, $(B-V)^{\rm Ty}$, $(V-J)$, $(V-H)$, and $(V-K_s)$ colours, and [Fe/H]. The total uncertainty $\sigma T_{\rm eff}^{\rm phot}$ was computed expanding the errors on colours, [Fe/H], and the internal uncertainty of the colour calibration given by the authors.

5.3. Consistency between spectroscopic and IRFM-photometric effective temperatures

The accuracy of effective temperature measurements and the consistency between temperature scales is a recurrent topic in stellar astrophysics, and its importance increased with the discovery of exoplanets and the arrival of precise data from large surveys. Spectroscopic and photometric scales show discrepancies for parameters far from solar (see e.g. comparisons in Casagrande et al. 2010; Heiter et al. 2015, and references in Table A.1).

Precise radius measurements from interferometry allow us to derive $T_{\rm eff}$ semidirectly for nearby stars, thus they can be used to test the accuracy of model-dependent techniques, for example by using the *Gaia Benchmark Stars* (Heiter et al. 2015). This task was performed by Giribaldi et al. (2019) for a parameter space similar to that analysed in this work. They found that the IRFM $T_{\rm eff}$ scale implemented by Casagrande et al. (2010) agrees with the interferometric scale, as already reported by Casagrande et al. (2014). On the other hand, they found that spectroscopic $T_{\rm eff}$ scales based in LTE + 1D model atmospheres present a bias as a function of [Fe/H], producing $T_{\rm eff}$ underestimations and overestimations respectively for metal-poor and metal-rich stars, regardless of line lists and particular implementations of the technique.

Giribaldi et al. (2019) showed a trend of the spectroscopic $T_{\rm eff}$ scale of Ghezzi et al. (2010a,b) with respect to $T_{\rm eff}$ based on interferometry as a function of [Fe/H], and provided corrections for it, that is, they empyrically converted this scale to the interferometric one (or to the IRFM one, which is equivalent). Our calibrations are based mainly on the same $T_{\rm eff}$ scale. In Fig. 5, we show the comparison between $T_{\rm eff}^{\rm phot}$ and the temperatures from the literature ($T_{\rm eff}^{\rm lit}$), which are essentially spectroscopic, for the calibration stars. We observe a similar trend to that shown by Giribaldi et al. (2019, their Fig. 10), and find that the equations they provide [4] subtract the trend. This equation is applied to $T_{\rm eff}^{\rm PCA}$ of the candidates, so the values listed in Table 2 are corrected values. These empirical corrections may be not elegant, but they are useful to confirm accurate $T_{\rm eff}$ for non-solar [Fe/H]. For example, they removed ∼50 K excess for the hot more metal-rich candidates HIP 10663 and HIP 75685, but they do not affect the $T_{\rm eff}$ of the solar analogues. The corrected $T_{\rm eff}^{\rm phot}$ and $T_{\rm eff}^{\rm PCA}$ values of the candidates are compared in Fig. 6, where $T_{\rm eff}^{\rm PCA}$ is used as the absolute scale in the abscissa due to its insensitivity to reddening. No trends are observed in the comparisons against $T_{\rm eff}$ and [Fe/H], and the offset between the two scales is practically null (we considered only the stars without any evidence of reddening to compute this difference; see Sect. 6 for details). This confirms the consistency of the corrected spectroscopic and photometric scales. Stars with significant temperature differences are highlighted by filled symbols in Fig. 6. Their associated reddening values are discussed in Sect. 6.

5.4. Effective temperature from Hα profiles

Once the consistency between spectroscopic and photometric scales is realized by applying corrections to $T_{\rm eff}^{\rm PCA}$, significantly cooler $T_{\rm eff}^{\rm phot}$ values suggest the presence of reddening. Here we verify by means of Hα profiles whether significant temperature differences are indeed due to reddening effects on $T_{\rm eff}^{\rm phot}$. Although the limited resolution of our spectra does not allow a

[4] Reduced into one equation here: $T_{\rm eff}^{\rm phot} = (T_{\rm eff}^{\rm lit} + 410)/1.08 - 153$[Fe/H] + 22, where $T_{\rm eff}^{\rm lit}$ represents the temperatures from the literature listed in Table A.1.

Table 2. Fundamental parameters of the observed faint solar analogue candidates.

HIP	Best $T_{\rm eff}$ (K)	$T_{\rm eff}^{\rm PCA} \pm 97$ (K)	$T_{\rm eff}^{\rm phot}$ (K)	[Fe/H] ± 0.06 (dex)	log g (dex)	Mass ($M_\odot$)	Radius ($R_\odot$)	Age (Gyr)
991	5829 ± 85	5750	5875 ± 74	−0.05	4.38 ± 0.06	0.99 ± 0.05	1.07 ± 0.05	6.2 ± 2.7
5811	5653 ± 67	5600	5696 ± 88	+0.02	4.39 ± 0.05	0.96 ± 0.05	1.04 ± 0.04	7.9 ± 2.6
6089	5684 ± 20	5669	5698 ± 95	−0.23	4.46 ± 0.04	0.90 ± 0.04	0.93 ± 0.03	6.9 ± 1.5
8853	6160 ± 50	6121	6192 ± 87	−0.17	4.32 ± 0.04	1.09 ± 0.05	1.20 ± 0.04	4.10 ± 1.0
10663	6125 ± 26	6140	6102 ± 120	−0.07	4.05 ± 0.03	1.24 ± 0.05	1.74 ± 0.04	4.4 ± 0.6
18941	5955 ± 90	6015	5887 ± 103	−0.29	4.39 ± 0.07	0.96 ± 0.06	1.04 ± 0.04	6.4 ± 2.9
[29100]	$T_{\rm eff}^{\rm PCA}$	6022	5824 ± 46	−0.33	4.49 ± 0.05	0.95 ± 0.05	0.92 ± 0.04	3.3 ± 2.3
31845	5705 ± 132	5785	5596 ± 113	−0.29	4.47 ± 0.06	0.89 ± 0.05	0.91 ± 0.04	7.2 ± 4.2
48272	5941 ± 14	5930	5950 ± 92	−0.36	4.40 ± 0.04	0.93 ± 0.05	1.01 ± 0.04	6.8 ± 0.9
55619	5686 ± 69	5758	5653 ± 65	−0.02	4.37 ± 0.05	0.96 ± 0.05	1.06 ± 0.04	8.0 ± 2.6
56870	5687 ± 108	5753	5599 ± 112	−0.28	4.49 ± 0.05	0.89 ± 0.05	0.89 ± 0.04	6.4 ± 4.0
61835	5895 ± 88	5848	5979 ± 132	−0.07	4.30 ± 0.05	1.02 ± 0.04	1.19 ± 0.05	7.1 ± 2.4
67692 (*)	–	–	5427 ± 37	−0.04	3.83 ± 0.04	1.23 ± 0.04	2.25 ± 0.06	5.2 ± 0.4
69477	5744 ± 49	5726	5812 ± 193	+0.02	4.46 ± 0.05	0.99 ± 0.05	0.98 ± 0.04	4.1 ± 2.7
[73234]	$T_{\rm eff}^{\rm PCA}$	5979	5775 ± 101	−0.17	4.28 ± 0.13	1.04 ± 0.06	1.22 ± 0.16	5.8 ± 2.0
[75685]	$T_{\rm eff}^{\rm PCA}$	6163	5515 ± 44	−0.02	4.40 ± 0.04	1.10 ± 0.04	1.10 ± 0.04	2.1 ± 1.5
107605	5835 ± 45	5809	5874 ± 120	−0.20	4.30 ± 0.03	0.95 ± 0.04	1.14 ± 0.04	0.95 ± 1.8
[**111826**]	$T_{\rm eff}^{\rm PCA}$	5655	5474 ± 47	+0.09	4.45 ± 0.06	0.98 ± 0.05	0.98 ± 0.04	5.0 ± 3.1

Notes. The first column lists the HIPPARCOS number. The three faint solar analogues with atmospheric parameters compatible with those of the Sun within 1σ errors are highlighted in large bold numbers, and the other three within 2σ errors in small bold numbers. The brackets indicate stars with suspected significant reddening values (see Table 3). Column 2 gives the best $T_{\rm eff}$ obtained by the weighted average of the values in Cols. 3 and 4. Column 3 displays $T_{\rm eff}^{\rm PCA}$ corrected by the equation given in Sect. 5.3. Column 4 displays $T_{\rm eff}^{\rm phot}$ from the photometric calibrations of Casagrande et al. (2010) and the colours in Table 1. Columns 5–9 to are self-explanatory. Three candidates listed in Table 1 are not listed here (HIP 13964, HIP 24742 and HIP 69232) because we could not derive their atmospheric parameters from PCA; their values lie outside the valid range of our calibrations. (*) $T_{\rm eff}^{\rm phot}$ and $T_{\rm eff}$ from Hα agree for this candidate. These values are out of the PCA applicability range, and $T_{\rm eff}^{\rm PCA}$ was found to be significantly hotter than $T_{\rm eff}^{\rm phot}$ and $T_{\rm eff}$ from Hα. No reddening was estimated for this candidate and we consider its atmospheric parameters as unreliable.

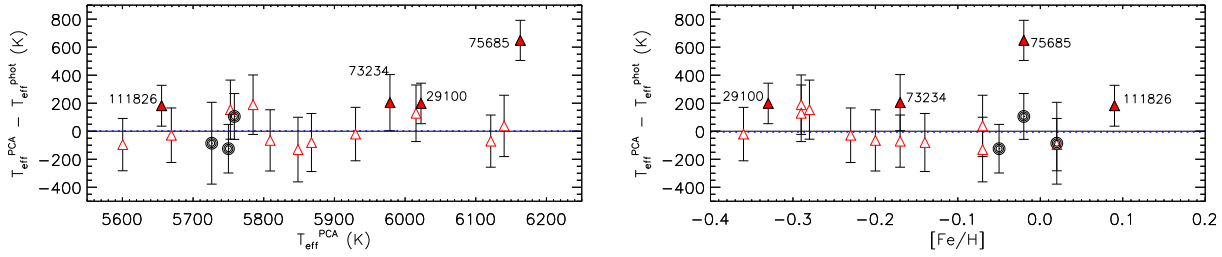

Fig. 6. Similar to the bottom panels of Fig. 5 for the candidates, but with $T_{\rm eff}^{\rm PCA}$ in the abscissa. Circles represent the stars in Table 2 with $T_{\rm eff}$, [Fe/H], and log g close to solar within 1σ errors, while triangles represent all other stars. Filled symbols represent the stars with significant temperature differences, they are also labelled by their HIP number. The dotted blue lines at −6 K represent the average $T_{\rm eff}$ difference, computed for the unlabelled stars only.

precise application of the Hα profile fitting and prevents the precise determination of $T_{\rm eff}$, temperature differences higher than ∼200 K are discernible.

The value of $T_{\rm eff}$ from Hα is not affected by reddening and its determination practically does not depend on other parameters at solar metallicity (e.g. Fuhrmann et al. 1993; Barklem et al. 2002). Its main source of error is the normalization, which is a complex task in high-resolution spectra, due to the narrow wavelength ranges that the profile leaves available in a spectral order for interpolating a polynomial that can reliably approximate the spectrograph response. However, our moderate resolution spectra are more than three times wider than the profile region, hence our normalization recovers the profile shape reasonably well. In Fig. A.1 we compare the observed profiles of HIP 67692 and HIP 75685 with synthetic profiles from the grid of Barklem et al. (2002), corresponding to temperatures similar to their $T_{\rm eff}^{\rm PCA}$ and $T_{\rm eff}^{\rm phot}$. This grid is found to be −28 K, accurate for the metallicity of these stars (Giribaldi et al. 2019). We also plot the observed profiles of other candidates with $T_{\rm eff}^{\rm PCA}$ values very similar to those of these two stars. The top plot in the figure shows that the profile of HIP 67692 is more compatible with its $T_{\rm eff}^{\rm phot}$, while the bottom plot favours $T_{\rm eff}^{\rm PCA}$ for HIP 75685, whose profile is slightly deeper than that of HIP 10663 with $T_{\rm eff}^{\rm PCA} \sim 6150$ K. Accordingly, $T_{\rm eff}^{\rm PCA} \sim 5400$ K for HIP 67692 is not listed in Table 2 since this value lies outside of the valid range of our index calibration.

5.5. Surface gravity, mass, and age

From the *Gaia* parallaxes (Gaia Collaboration 2018), plus the best $T_{\rm eff}$, and [Fe/H] values shown in Tables 1 and 2, we calculated stellar luminosities using bolometric corrections from

Andrae et al. (2018) and extinction values from our reddening estimates in Table 3. Surface gravity, mass, and age were obtained from theoretical evolutionary tracks of Kim et al. (2002) and Yi et al. (2003) following the procedure described in Grieves et al. (2018).

6. Reddening

The hunt for solar analogues begins, necessarily, by selecting candidates with solar photometric colours, as they are the most direct observational parameters able to quantify similarities between stars. Once stars with photometry equal to solar produced by the degeneracy of the atmospheric parameters (principally $T_{\rm eff}$–[Fe/H]) are identified and discarded, solar-like colours should lead to stars with the same atmospheric parameters as the Sun. However, in the presence of interstellar extinction a star that presents observed reddened colours equal to solar will have different combinations of atmospheric parameters and will tend to be hotter than the Sun. For hunters of solar analogues and twins at large distances, this implies that reddening corrections must be considered. For users of solar proxies, it also means that regardless of whether the intrinsic atmospheric parameters of a star are solar, the observed colours will always be reddened, i.e. $B{-}V_\star > B{-}V_\odot$. Therefore, a faint star with apparent solar colours will have a flux distribution different from solar, and when used to remove the solar spectral signature from the spectrum of the target, it will introduce systematic trends in its spectral albedo.

We estimate reddening values for the candidates for which $T_{\rm eff}^{\rm phot}$ are smaller than $T_{\rm eff}^{\rm PCA}$. These are shown as filled triangles in Fig. 6. The colour excess $E(B{-}V) = (B{-}V)_{\rm reddened} - (B{-}V)_{\rm intrinsic}$ is then computed by the difference between the colour required to obtain the average $T_{\rm eff}^{\rm phot}$ and that required to obtain $T_{\rm eff}^{\rm PCA}$ by using the calibrations of Casagrande et al. (2010). Since $T_{\rm eff}^{\rm phot}$ was determined by the weighted average of several colours, $(B{-}V)_{\rm reddened}$ values are not exactly the same as those in Table 1. Table 3 shows $E(B{-}V)$ estimated by this method; they can be considered as lower limit estimates of the actual reddening in $B{-}V$ since this actual reddening is somewhat diluted by the process of determining the average $T_{\rm eff}^{\rm phot}$ also employing colours that are less affected by reddening than $B{-}V$.

Extinction models

We compare here our $E(B{-}V)$ estimates with those predicted by two extinction maps. Reddening estimations by other methods such as Ca II H & K lines, Na I D lines (e.g. Alves-Brito et al. 2010; Curtis 2017), and diffuse interstellar bands (Law et al. 2017) were not possible due to the limitations established by the resolution and wavelength coverage of our spectra. The description of dust distribution in our Galaxy has progressed a lot over the last two decades for both 2D and 3D maps and models (Robin et al. 2015; Sale 2015). Schlegel et al. (1998, hereafter SFD) published 2D maps based on the far-IR (FIR) emission detected by the COBE/DIRBE satellite. This model was reviewed by Beers et al. (2002, hereafter SFD-B) in order to correct overestimations of the total reddening in internal regions of the Galaxy.

Amôres & Lépine (2005, hereafter A&L) presented two models for interstellar extinction in the Galaxy that take into account the gas distribution for HI and HII. In the first model, the Galaxy is axisymmetric (ALA) and extinction increases linearly as function of distance. In the second model (ALS), the spiral structure is considered and the extinction increases by steps each time a spiral arm is crossed. They compared their models for a wide range of distances and directions by using some catalogues, such as Neckel & Klare (1980), Savage et al. (1985), and Guarinos (1992). The last catalogue has the majority of their stars located at distances up to 500 pc.

Arce & Goodman (1999), and A&L among other works, find that SFD overestimates extinction for $E(B{-}V) \sim 0.15$ mag. Some simplifications made in the map such as resolution and the unique value used for dust temperature are provided as explanations for the overestimations. The overestimations are expected to mainly affect the Galactic plane and towards molecular clouds, however, distance from which they start to be relevant has not been explored.

Our choice was to use the ALA model of A&L and the SFD-B model to test their consistency with our estimates from $T_{\rm eff}^{\rm PCA} - T_{\rm eff}^{\rm phot}$ at ~170 pc, their $E(B{-}V)$ are listed in Table 3. Figure 7 shows $E(B{-}V)$ from A&L and SFD-B for all candidates plotted against $T_{\rm eff}^{\rm PCA} - T_{\rm eff}^{\rm phot}$ from dereddened colours (red triangles), and also from non-dereddened colours (blue bars) for the reader to check the corresponding temperature corrections. $E(B{-}V)$, $E(B{-}V)^{\rm Ty}$, $E(V{-}J)$, $E(V{-}H)$, and $E(V{-}K)$ were

Table 3. Colour excess values $E(B{-}V)$ of candidates with significant $T_{\rm eff}^{\rm phot}$ underestimations, compared with predictions from the SFD, SFD-B, and A&L models plus our own estimate in Col. 4.

HIP	SFD	SFD-B	A&L	This work	$\Delta T_{\rm eff}$ (K)
29100	0.0426	0.0136	0.0104	0.058 ± 0.042	198
73234	0.0244	0.0244	0.0206	0.062 ± 0.061	204
75685	0.1647	0.0963	0.0221	0.203 ± 0.043	648
111826	0.0290	0.0290	0.0104	0.063 ± 0.051	182

Notes. The last column gives the $T_{\rm eff}^{\rm phot}$ underestimation with respect to $T_{\rm eff}^{\rm PCA}$ implicated by the values in Col. 4.

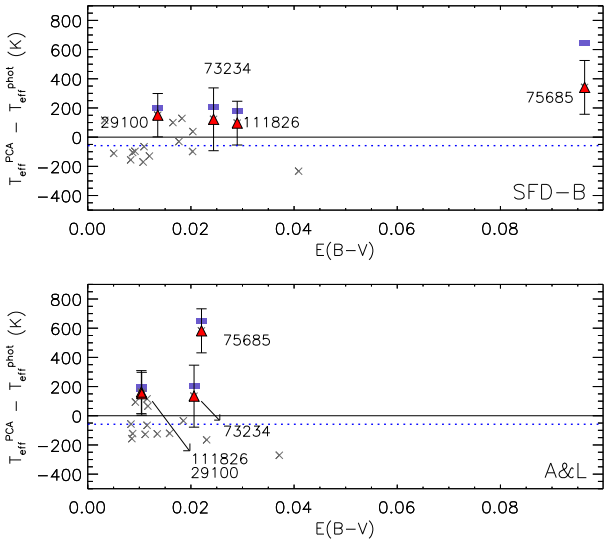

Fig. 7. Difference between spectroscopic $T_{\rm eff}^{\rm PCA}$ and dereddened $T_{\rm eff}^{\rm phot}$ of candidates according to the extinction models by SFD-B (*top panel*) and A&L (*bottom panel*). The stars with no significant differences are represented by crosses, and the others by the same symbols as in Fig. 6. As a reference, temperature differences from undereddened colours are indicated by blue symbols, i.e. the same values as in Fig. 6. In both plots, the dotted lines at approximately −50 K represent the average $T_{\rm eff}^{\rm PCA} - T_{\rm eff}^{\rm phot}$ of the stars represented by the crosses.

considered to obtain dereddened $T_{\rm eff}^{\rm phot}$; the same values were used for Johnson and *Tycho*, while 2MASS reddenings were converted from Johnson by the relations given by Zagury & Turner (2012) for $R_V = 3.14$ mag. The errors of dereddened $T_{\rm eff}^{\rm phot}$ were estimated expanding those of $E(B-V)$ given by the models, colours, parallax, [Fe/H], and photometric calibrations. These errors proved to be practically the same as those from non-dereddened $T_{\rm eff}^{\rm phot}$ because the error budget is dominated by parallax errors, which are negligible for the *Gaia* data in our distance range.

Both models remove (or at least minimize) the differences of the labelled stars, except for HIP 75685. For this case, SFD-B predicts a substantially higher $E(B-V)$ than A&L, but still lower than our estimate $E(B-V)$ of ∼0.20 mag. This value agrees with that of SFD, which is the total reddening predicted by the model for the line of sight, although it is in the range where the model predictions are known to present problems ($E(B-V) > 0.15$ mag) as pointed out above. Given the reasonable agreement between these independent estimates of reddening, we consider the case for these three objects as substantial, particularly for HIP 75685.

7. Best faint solar analogues

The results of the previous sections point towards the identification of a sample of faint solar analogues of $V \sim 10.5$ mag which reproduce well the atmospheric parameters of the Sun and should be good matches for its spectrophotometric flux distribution for a wide range of wavelengths. Three stars have atmospheric parameters agreeing with solar within 1σ of their formal errors: HIP 991, HIP 5811 and HIP 69477. Two other candidates also agree in the same sense but within 2σ of their errors: HIP 55619 and HIP 61835. Their ages are found to be comparable or larger than the Sun's, and moreover their Hα line cores do not show any discernible fill-in from a high level of chromospheric activity, which should be apparent even in moderately low-resolution spectra (Lyra & Porto de Mello 2005). All the evidence points to their being middle-aged, inactive solar analogues. Their estimated masses and radii also closely match the solar ones within formal uncertainties, but HIP 61835 which has a slightly larger radius. They are reasonably well distributed across the sky but slightly biased towards southern declinations due to the reach of our observations.

Six additional objects have $T_{\rm eff}$ values matching the solar value but appear as slightly metal−poor in the $-0.30 < [{\rm Fe/H}] < -0.20$ dex range. They are probably poorer solar matches for shorter wavelengths, but should reproduce the Sun increasingly better towards redder spectral ranges and are probably very good in the infrared (Porto de Mello et al. 2014). These are HIP 6089, HIP 18941, HIP 31845, HIP 48272, HIP 56870, and HIP 107605. Consistently with their more diverse atmospheric parameters, their masses and radii do not match the Sun's as closely as the best analogues, but all of them (except HIP 107605) appear to be old stars and thus are free from a high degree of chromospheric activity, and are also reasonably well scattered in the sky. These stars may be considered by potential users to be reasonable matches to the Sun as a function of the desired precision and accuracy for the target observations. All 11 of the above-mentioned faint solar analogues are free from any evidence of reddening according to our analysis. We could not find any sign of binarity in the spectra of the candidates analysed, and better quality observations should be used to eliminate this possibility.

8. Conclusions

Motivated by the demand for faint spectrophotometric solar analogues, we implemented the methodologies to derive atmospheric parameters with optimized precision from moderately low-resolution and S/N spectra. We selected a sample of candidates with $V \sim 10.5$ mag in the HIPPARCOS catalogue by matching the solar M_V and $B-V$ values in the Johnson and *Tycho* systems; subsequently we submitted a subsample of them to spectroscopic analysis. The method for deriving atmospheric parameters consist of a system of 24 spectral indices, whose sensitivity to $T_{\rm eff}$ and [Fe/H] were mathematically modeled by the PCA regression. The models were based on published spectroscopic $T_{\rm eff}$ values (based on the excitation and ionization equilibrium of Fe lines in LTE + 1D model atmospheres), thus $T_{\rm eff}$ derived by the spectral indices may be also deemed spectroscopic. Considering the discrepancies between $T_{\rm eff}$ scales from different techniques at parameters far from solar, we assured the consistency of the spectroscopic $T_{\rm eff}$ with the photometric $T_{\rm eff}$ (Casagrande et al. 2010), which is consistent with the interferometric $T_{\rm eff}$ of the *Gaia Benchmark Stars* (Heiter et al. 2015), using the relations given by Giribaldi et al. (2019). The corrected spectroscopic $T_{\rm eff}$ values are shown to match the photometric values. Except for the stars showing evidence of reddening, the adopted $T_{\rm eff}$ values were derived by averaging the photometric and spectroscopic determinations.

The derived spectroscopic $T_{\rm eff}$ and [Fe/H] have internal precision of 97 K and 0.06 dex, respectively. The PCA index system is very successful in recovering atmospheric parameters with good precision for low S/N spectra, and may be used to study fainter stars in large databases; the accuracy of these parameters entirely relies on the accuracy of the calibrating sample. The method implemented here deals with the spectra of dwarf stars acquired by large telescopes, which correspond to $V = 16$–18 mag, for original or degraded resolutions similar to those used here.

Surface gravities, masses, radii, and ages were derived from the finally adopted atmospheric parameters and *Gaia* parallaxes by means of theoretical evolutionary tracks and isochrones (Kim et al. 2002; Yi et al. 2003). We identified 11 solar analogues with different degrees of resemblance to the Sun: their individual suitability as solar surrogates is judged in Sect. 7. Their fundamental parameters, and those of other candidate stars that did not fully meet the requirements as solar analogues are listed in Table 2; their photometric and astrometric parameters are listed in Table 1.

Initial candidates lie between 90 pc and 290 pc, and we estimated reddening for them independently from published extinction models, by comparing photometric $T_{\rm eff}$ with corrected spectroscopic $T_{\rm eff}$, since corrected spectroscopic $T_{\rm eff}$ values are shown to be consistent with photometric values. We find evidence of significant reddening for four candidates that present significant cooler photometric $T_{\rm eff}$. A common reddening value at these distances resulted in $E(B-V) \sim 0.06$ mag, which translates to a ∼200 K decrease in photometric $T_{\rm eff}$. Our estimates are validated by predictions from the SFD-B and A&L extinction models, except for one star, HD 75685, which appears to lie in a very dense region.

The identified analogues have no evidence of reddening, and may be used photometrically and spectroscopically for subtracting the solar signature with good precision from observations of solar system bodies. In the visible and infrared regions they should present a very good match to the Sun, even in the UV up to 4000 Å. Our reddening analysis shows that solar analogue

candidates will be progressively more affected by reddening. These stars will present spectra and colours that appear to belong to cooler stars as they become fainter (or more affected by reddening), as seems to be the case of HIP 75685. As future generations of larger telescopes increase the demand for faint stars matching the solar spectra, this will become a relevant issue to be addressed for the very faint solar analogues: photometrically selected solar analogues will not match the actual spectroscopic properties of the Sun.

Acknowledgements. R.E.G. acknowledges scholarships from CAPES and ESO, G.F.P.M. acknowledges grant 474972/2009-7 from CNPq/Brazil, D.L.S. acknowledges a scholarship from CAPES and FAPESP 2016/20667-8, and M.L.U.M. acknowledges scholarships from FAPERJ and CAPES. We thank the staff of the OPD/LNA for considerable support in the many observing runs carried out during this project. We also thank the anonymous referee for the helpful and constructive criticism to this work. Use was made of the Simbad database, operated at the CDS, Strasbourg, France, and of NASA's Astrophysics Data System Bibliographic Services. This publication makes use of data products from the Two Micron All Sky Survey, which is a joint project of the University of Massachusetts and the Infrared Processing and Analysis Center/California Institute of Technology, funded by the National Aeronautics and Space Administration and the National Science Foundation. This work presents results from the European Space Agency (ESA) space mission *Gaia*. The *Gaia* data are being processed by the *Gaia* Data Processing and Analysis Consortium (DPAC). Funding for the DPAC is provided by national institutions, in particular the institutions participating in the *Gaia* MultiLateral Agreement (MLA). The *Gaia* mission website is `https://www.cosmos.esa.int/gaia`. The *Gaia* archive website is `https://archives.esac.esa.int/gaia`.

References

Adibekyan, V. Z., Figueira, P., Santos, N. C., et al. 2013, A&A, 554, A44
Alvarez-Candal, A., Fornasier, S., Barucci, M. A., de Bergh, C., & Merlin, F. 2008, A&A, 487, 741
Alves-Brito, A., Meléndez, J., Asplund, M., Ramírez, I., & Yong, D. 2010, A&A, 513, A35
Amôres, E. B., & Lépine, J. R. D. 2005, AJ, 130, 659
Andrae, R., Fouesneau, M., Creevey, O., et al. 2018, A&A, 616, A8
Arce, H. G., & Goodman, A. A. 1999, ApJ, 512, L135
Barklem, P. S., Stempels, H. C., Allende Prieto, C., et al. 2002, A&A, 385, 951
Beck, P. G., do Nascimento, Jr. J.-D., Duarte, T., et al. 2017, A&A, 602, A63
Beers, T. C., Drilling, J. S., Rossi, S., et al. 2002, AJ, 124, 931
Bensby, T., Feltzing, S., & Lundström, I. 2003, A&A, 410, 527
Blackwell, D. E., & Shallis, M. J. 1977, MNRAS, 180, 177
Blackwell, D. E., Shallis, M. J., & Selby, M. J. 1979, MNRAS, 188, 847
Blackwell, D. E., Petford, A. D., & Shallis, M. J. 1980, A&A, 82, 249
Blanco-Cuaresma, S., Soubiran, C., Heiter, U., et al. 2015, A&A, 577, A47
Casagrande, L., Ramírez, I., Meléndez, J., Bessell, M., & Asplund, M. 2010, A&A, 512, A54
Casagrande, L., Portinari, L., Glass, I. S., et al. 2014, MNRAS, 439, 2060
Cayrel de Strobel, G. 1996, A&ARv, 7, 243
Chapman, C. R., Morrison, D., & Zellner, B. 1975, Icarus, 25, 104
Curtis, J. L. 2017, AJ, 153, 275
Cutri, R. M., Skrutskie, M. F., van Dyk, S., et al. 2003, 2MASS All Sky Catalog of point sources
da Silva, L., & Porto de Mello, G. F. 2000, IAU Symp., 198, 495
da Silva, R., Milone, A. C., & Reddy, B. E. 2011, A&A, 526, A71
da Silva, R., Porto de Mello, G. F., Milone, A. C., et al. 2012, A&A, 542, A84
Do Nascimento, Jr. J. D., Castro, M., Meléndez, J., et al. 2009, A&A, 501, A687
Dumas, C., Carry, B., Hestroffer, D., & Merlin, F. 2011, A&A, 528, A105
Fernley, J., Neckel, H., Solano, E., & Wamsteker, W. 1996, A&A, 311, 245
Fuhrmann, K., Axer, M., & Gehren, T. 1993, A&A, 271, 451
Gaia Collaboration (Brown, A. G. A., et al.) 2016a, A&A, 595, A2
Gaia Collaboration (Prusti, T., et al.) 2016b, A&A, 595, A1
Gaia Collaboration (Brown, A. G. A., et al.) 2018, A&A, 616, A1
Galarza, J. Y., Meléndez, J., & Cohen, J. G. 2016, A&A, 589, A65
Ghezzi, L., Cunha, K., Schuler, S. C., & Smith, V. V. 2010a, ApJ, 725, 721
Ghezzi, L., Cunha, K., Smith, V. V., et al. 2010b, ApJ, 720, 1290
Ghezzi, L., Dutra-Ferreira, L., Lorenzo-Oliveira, D., et al. 2014, AJ, 148, 105
Giribaldi, R. E., Ubaldo-Melo, M. L., Porto de Mello, G. F., et al. 2019, A&A, 624, A10
Gordon, K. D., Clayton, G. C., Misselt, K. A., Land olt, A. U., & Wolff, M. J. 2003, ApJ, 594, 279
Grieves, N., Ge, J., Thomas, N., et al. 2018, MNRAS, 481, 3244
Guarinos, J. 1992, in European Southern Observatory Conference and Workshop Proceedings, eds. A. Heck & F. Murtagh (Cambridge: Cambridge University Press), 43, 301
Hardorp, J. 1982, A&A, 105, 120
Heiter, U., Jofré, P., Gustafsson, B., et al. 2015, A&A, 582, A49
Hoeg, E., Bässgen, G., Bastian, U., et al. 1997, A&A, 323, L57
Hunt, L., Magrini, L., Galli, D., et al. 2012, MNRAS, 427, 906
Jurić, M., Ivezić, Ž., Brooks, A., et al. 2008, ApJ, 673, 864
Kim, Y.-C., Demarque, P., Yi, S. K., & Alexander, D. R. 2002, ApJS, 143, 499
Kurucz, R. L. 2005, Mem. Soc. Astron. It. Suppl., 8, 189
Law, C. J., Milisavljevic, D., Crabtree, K. N., et al. 2017, MNRAS, 470, 2835
Li, T. D., Bi, S. L., Liu, K., Tian, Z. J., & Shuai, G. Z. 2012, A&A, 546, A83
Luck, R. E., & Heiter, U. 2006, AJ, 131, 3069
Lyra, W., & Porto de Mello, G. F. 2005, A&A, 431, 329
Meléndez, J., Dodds-Eden, K., & Robles, J. A. 2006, ApJ, 641, L133
Meléndez, J., Schirbel, L., Monroe, T. R., et al. 2014, A&A, 567, L3
Merlin, F., Hromakina, T., Perna, D., Hong, M. J., & Alvarez-Candal, A. 2017, A&A, 604, A86
Moore, C. E., Minnaert, M. G. J., & Houtgast, J. 1966, The solar spectrum 2935 A to 8770 A (Washington: US Government Printing Office)
Muñoz Bermejo, J., Asensio Ramos, A., & Allende Prieto C. 2013, A&A, 553, A95
Neckel, T., & Klare, G. 1980, A&AS, 42, 251
Önehag, A., Korn, A., Gustafsson, B., et al. 2011, A&A, 528, A85
Pasquini, L., Biazzo, K., Bonifacio, P., et al. 2008, A&A, 489, 677
Perryman, M. A. C., Lindegren, L., Kovalevsky, J., et al. 1997, A&A, 323, L49
Porto de Mello, G. F., & da Silva, L. 1997, ApJ, 482, L89
Porto de Mello, G. F., da Silva, R., da Silva, L., & de Nader, R. V. 2014, A&A, 563, A52
Prša, A., Harmanec, P., Torres, G., et al. 2016, AJ, 152, 41
Ramírez, I., Meléndez, J., & Asplund, M. 2009, A&A, 508, L17
Robin, A. C., Marshall, D., Reylé, C., & Montillaud, J. 2015, Mem. Soc. Astron. It., 86, 579
Ryabchikova, T., Piskunov, N., Kurucz, R. L., et al. 2015, Phys. Scr, 90, 054005
Sale, S. E. 2015, Mem. Soc. Astron. It., 86, 568
Savage, B. D., Massa, D., Meade, M., & Wesselius, P. R. 1985, ApJS, 59, 397
Schlegel, D. J., Finkbeiner, D. P., & Davis, M. 1998, ApJ, 500, 525
Snodgrass, C., Yang, B., & Fitzsimmons, A. 2017, A&A, 605, A56
Soubiran, C., & Triaud, A. 2004, A&A, 418, 1089
Tholen, D. J., & Barucci, M. A. 1989, in Asteroids II, eds. R. P. Binzel, T. Gehrels, & M. S. Matthews (Tucson: University of Arizona Press), 298
Yi, S. K., Kim, Y.-C., & Demarque, P. 2003, ApJS, 144, 259
Zagury, F., & Turner, D. G. 2012, Astron. Nachr., 333, 640

Appendix A: Additional material

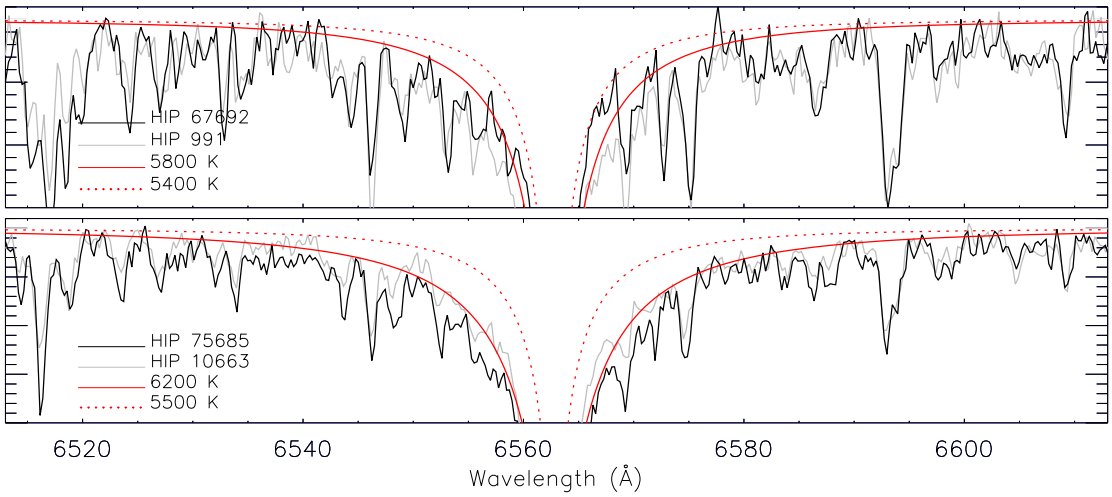

Fig. A.1. Hα profiles of HIP 67692 (*top*) and HIP 75685 (*bottom*) compared to synthetic profiles with temperatures similar to their $T_{\rm eff}^{\rm PCA}$ (full line) and $T_{\rm eff}^{\rm phot}$ (dotted line). The observed profile of another candidate with a similar $T_{\rm eff}^{\rm PCA}$ value on each profile (in grey).

Table A.1. Atmospheric parameters of the calibration stars.

HD	$T_{\rm eff}$ (K)	[Fe/H]	log g	Author	S/N
1461	5717	0.17	4.33	1	155
1581	5908	−0.20	4.26	1	166
2151	5866	−0.11	4.00	1	324
4391	5829	−0.08	4.45	8	201
7570	6196	0.24	4.41	1	297
8291	5835	0.03	4.30	2	141
9562	5794	0.16	3.95	1	217
9986	5820	0.09	4.48	2	297
10647	6155	−0.06	4.44	1	223
10700	5321	−0.56	4.46	1	471
12264	5810	0.06	4.54	2	194
16417	5788	0.14	4.05	1	272
17051	6239	0.16	4.55	1	269
19994	6081	0.08	4.07	1	192
20010	6280	−0.02	4.26	7	368
20029	6184	0.07	4.31	1	224, 170
20630	5723	0.09	4.36	1	274
30495	5740	0.09	4.36	5	237
30562	5986	0.27	4.30	5	424
34721	5957	−0.10	4.21	5	177, 252
36553	6022	0.27	3.73	5	498
39091	6037	0.08	4.42	1	207
39587	6029	−0.01	4.62	1	426
43587	5950	0.01	4.36	5	109
43947	5889	−0.27	4.32	1	117
52298	6253	−0.31	4.41	1	204
65907	6027	−0.31	4.57	1	320
98649	5775	−0.02	4.44	2	151
105901	5845	−0.01	4.54	2	117
112164	6014	0.32	4.05	3	131, 228
115382	5775	−0.08	4.40	2	106
117939	5608	−0.26	4.19	1	230
118598	5755	0.02	4.44	2	169
131117	5904	0.10	3.96	1	135, 184
134060	5904	0.10	4.25	1	149
138573	5750	0.00	4.41	2	294
146233	5795	−0.03	4.42	2	313, 310
147584	6090	−0.06	4.45	6	332
150248	5687	−0.11	4.30	1	486, 134
156274	5242	−0.37	4.40	1	163
157089	5785	−0.47	4.09	1	182
159656	5845	0.09	4.32	2	357
160691	5695	0.23	4.02	1	263
162396	6026	−0.37	4.08	1	39
164595	5790	−0.04	4.44	2	147
172051	5502	−0.16	4.43	5	496
182572	5569	0.40	4.10	4	449
187237	5850	0.16	4.48	2	284
189567	5656	−0.26	4.20	1	431
190248	5691	0.39	4.26	1	273
193307	6018	−0.34	4.18	1	341
196378	5996	−0.44	3.92	1	409
196755	5639	0.04	3.70	1	243
199288	5724	−0.60	4.55	1	227
199960	5940	0.27	4.26	7	326
203608	6022	−0.67	4.31	1	214
205420	6255	0.00	3.89	1	450, 171
206395	6305	0.23	4.38	1	256, 269
206860	6106	−0.04	4.68	4	247
207043	5775	0.07	4.55	2	276
210918	5721	−0.09	4.27	1	161
211415	5753	−0.25	4.27	5	202
212330	5670	−0.02	3.91	1	279, 232
215648	6178	−0.027	3.97	1	451, 301
216436	5755	0.04	3.94	2	70
221287	6241	−0.02	4.37	1	236
221343	5755	0.04	4.05	2	177
222368	6200	−0.02	4.13	1	810
BD+15 3364	5785	0.07	4.44	2	175

Notes. The first column lists the HD number, except for the last star. Columns 2, 3, and 4 are the atmospheric parameters. Column 6 gives the S/N; both values are when there are two observations for one star.

References. Literature source coded by number: 1. Ghezzi et al. (2010a,b), 2. Porto de Mello et al. (2014), 3. da Silva et al. (2012), 4. da Silva et al. (2011), 5. da Silva & Porto de Mello (2000), 6. Bensby et al. (2003), 7. Luck & Heiter (2006), 8. Lyra & Porto de Mello (2005).